Original Research Paper

Cold-pressing and vacuum arc melting of γ-TiAl based alloys

M.N. Mathabathe[a, b, *]

nmathabathe@csir.co.za

A.S. Bolokang[b, c, **]

sbolokang@csir.co.za

G. Govender[b]

C.W. Siyasiya[a]

R.J. Mostert[a]

[a]Department of Material Science and Metallurgical Engineering, Faculty of Engineering, Built Environment and Information Technology, University of Pretoria, South Africa

[b]Council of Scientific Industrial Research, Materials Science and Manufacturing, Manufacturing Cluster, Light Metals, Meiring Naude Road, PO Box 395, Pretoria, South Africa

[c]Department of Physics, University of the Western Cape, Private Bag X 17, Bellville 7535, South Africa

*Corresponding author at: Department of Material Science and Metallurgical Engineering, Faculty of Engineering, Built Environment and Information Technology, University of Pretoria, South Africa.

**Corresponding author at: Council of Scientific Industrial Research, Materials Science and Manufacturing, Manufacturing Cluster, Light Metals, Meiring Naude Road, PO Box 395, Pretoria, South Africa.

Abstract

Beta (β) solidifying γ-TiAl intermetallic alloys of nominal composition Ti-48Al, Ti-48Al-2Nb, Ti-48Al-2Nb-0.7Cr alloys have been cold pressed and vacuum arc melted. The Al loss was due to compaction method used prior to the melting technique, since it was evident after compaction that Al particles migrated to the surface in contact with the die facets after cold pressing. Electron backscatter diffraction (EBSD)-orientation mapping demonstrated that the α-precipitation from the parent β-phase follows the Blackburn orientation relationship (BOR). Microstructural characterization of the alloys was studied by scanning electron microscopy (SEM) equipped with energy dispersion spectroscopy (EDS) for micro-analysis. X-ray diffraction (XRD) technique was used to detect phase compositions.

Keywords: Uniaxial cold pressing; Vacuum arc melting (VAM); γ-TiAl based alloys; β-phase domain

1 Introduction

TiAl-based alloys are promising materials for high-temperature applications due to their low density, high specific strength, stiffness, oxidation resistance. However, the alloys suffer from inherent poor ductility and toughness at room temperature [1]. Therefore, improvement of the TiAl alloys will be appreciated by the industry where they play a critical role. Despite the excellent intermetallic γ-TiAl based alloys properties, their intrinsic lack of hot deformability poses major challenges in the fabrication of complex geometries using the most of conventional processing methods hence becoming impractical to produce sound products [2–5]. It is crucial to address issues around microstructure evolution and material processing which plays a crucial role in making modern jet engines a reality. In the manufacture of γ-TiAl based alloys the castability is essential for industrial application as many of these alloy components are synthesised by casting. However, cost of production is increased by a large number of casting defects which makes their application challenging. The basic problems faced by the investment casting microstructures as an example was explained in the work done by Dey et al. [2], i.e. producing coarse lamellar structures as a result of sharp solidification texture with anisotropic properties and low room temperature ductility. However, the authors further reported that $(\alpha_2 + \gamma)$ lamellar grains with fine lamellae spacing are a solution to these problems. In addition, Yang et al. [3] reported that TiAl-based alloys have a lower castability, high chemical reactivity and larger solidification shrinkage rate than typical Al casting alloys, of which not only causes misrun defects on the surface of the components but also results in shrinkage porosity and crack defects with poor ductility. For obtaining the sound quality of castings, it is necessary to select appropriate casting process and technological parameters. However, according to Franzen and Karlsson [4] reported that coarse microstructure and segregation obtained in castings could be avoided by employing powder metallurgy with rapid solidification; of which the solidification microstructure can be refined, homogeneous and therefore comparable to wrought material. In addition, green strength plays a vital role in powder metallurgical processing. Green strength refers to the mechanical strength of a cold-pressed powder compact. The strength of green compacts results mainly from mechanical interlocking of irregularities on the particle surfaces, which is promoted by plastic deformation during pressing [5]. Fang et al. [6] reported that powder metallurgy (PM) manufacturing technique, especially the blended elemental powder metallurgy (BEPM) approach to alloying, is a viable and promising route for the cost-effective fabrication of titanium components. Therefore, it is of vital importance to incorporate powder metallurgy route with that of the ingot metallurgy technique as it may be a potential fabrication process in producing defect-free alloy products. Vacuum arc remelting (VAR) is a process for melting metals which has been developed in 1839. However, its wild use for manufacturing structural materials began after world war two. It was common practice that VAR was the process that followed vacuum induction melting (VIM). The reason for this sequence was that VIM establishes close control of alloy formation and chemistry, whereas the VAR exhibits the desired microstructure due to greater control of solidification rate. As a result, VAR ingots are generally of higher bulk density than are VIM ingots. In addition, refractory-line VIM furnaces are not suitable for Ti alloys due to high melting and reactivity of Ti with most ceramics which results in brittle inclusions. These problems that are related to melting and alloy synthesis of Ti alloys were resolved by the development of non-consumable electrode arc melting in a water-cooled copper crucible, where the first molten Ti to solidify forms a thin protective layer known as the skull. VAR became widely used which was producing acceptable products to date, respectively [7]. According to Shen et al. [8] the manufacturing of TiAl based sheets in terms of ingot metallurgy (IM), and the powder metallurgical (PM) routes have been well established in the variety of systems. However, in the use of IM approaches the authors emphasized that cast ingots must undergo thermos-mechanical processing such as hot isostatic pressing (HIPing) prior to hot rolling. The Ti-48Al-2Nb-0.7Cr-0.3Si alloy exhibited good mechanical properties when compared to the Ti-48Al, Ti-48Al-2Nb, and Ti-48Al-2Nb-0.7Cr alloys [9] while the surface nitridation of Ti-48Al-2Nb-0.7Cr significantly improved its cyclic oxidation and the best performance at 900 °C after 900 h (h) [10]**.** The aim of the cuurent work was to investigate the vacuum arc melting (VAR) of the compacted alloy powders was used for fabrication of the Ti-48Al, Ti-48Al-2Nb, and Ti-48Al-2Nb-0.7Cr alloys with minimal loss of volatile Al. The binary (Ti-48Al), ternary (Ti-48Al-2Nb) and quaternary (Ti-48Al-2Nb-0.7Cr) alloys in (at.%) were developed by combining both powder and ingot metallurgy routes via uniaxial cold pressing. Understanding of the particle arrangement during cold pressing and effect of melting on the Al content of the as-cast β-solidified γ-TiAl alloys was considered.

2 Experimental work

2.1 Elemental powder preparation

Pure precursor Ti, Al, Nb and Cr elemental powders were mixed and blended with subsequent cold pressing and arc melting in the vacuum of 1×10^{-5} Torr using a small electric arc button furnace, in order to synthesize Ti-48Al, Ti-48Al-2Nb, and Ti-48Al-2Nb-0.7Cr (at.%) alloys. The detailed fabrication process is similar to the one reported in [9].

2.2 Uniaxial cold pressing

The cold pressing was done using the Enerpac hydraulic press with 380 MPa pressure applied on powder specimens. Succeeding uniaxial cold pressing, the vacuum arc melting operation also reported in [9], yielded the ingots in the form of buttons. Chemical analysis of the button alloys was performed using inductively coupled plasma emission optical spectroscopy (ICP-EOS). The final chemical composition of the alloys after melting is shown in Table 1 previously addressed in [9]. Therefore the experimental results are reproducible, and the achieved findings verified independently.

Table 1 As-vacuum final chemical composition (at.%) [9].

Alloy	Ti	Al	Nb	Cr
Binary	55.7	44.3	–	–
Ternary	52.38	45.82	1.8	–
Quaternary	51.04	46.41	1.89	0.73

2.3 Materials characterization

Metallographic preparation of the alloys was carried out using an optical microscope (OM) and scanning electron microscope (SEM) to reveal the microstructure of the alloys. The SEM is a JEOL® JSM-6510 instrument model which was conducted in a backscattered electron (BSE) and secondary electron image (SEI) mode equipped with energy dispersive X-ray spectroscopy (EDS) capabilities for micro-analysis, likewise, the calibration technique is similar to the one explained in [9]. In addition, the SEM-EBSD technique was employed for microstructure characterisation. The structural phase evolution was characterized by X-ray diffraction technique with Cu Kα radiation λ = 1.54062 Å and 2θ from 20° to 90°. Specimens were ground and polished using 1 µm diamond suspension, followed by final polishing using 50 nm colloidal silica. Vickers hardness tests were conducted according to the requirements of ASTM standards E384-10. The density of the as-compacted and as-melted alloy parts was measured using the Archimedes method according to ASTM B962-08.

3 Results and discussion

3.1 Precursor elemental powders

Fig. 1a–d shows the SEM micrographs of the Ti, Al, Nb and Cr powder particles, respectively. Ti, Nb, and Cr powder particles illustrate the angular but irregular shape with various particle sizes. The average particles sizes are 30.51 µm, 23.89 µm and 126 µm for Ti, Nb and Cr powders. The Al elemental powder illustrate a spherical morphology comprising of varying particle sizes. It seems that the smaller particle-droplets have agglomerated to form large particle sizes in Al powder. The average particle sizes of 74 µm were measured. The powder particle sizes are summarised in Table 2. The particles distribution curves in Fig. 2a–d are in agreement with the SEM analysis. Al powder shows a narrow particle distribution compared to Ti, Nb and Cr powder particles, this may be due to the spherical morphology of the elemental powder. The physical properties of the elemental powders are presented in Table 3 below. These elemental properties contribute to the final Ti-48Al-2Nb-0.7Cr alloy after chemical reaction during melting and casting amid alloy formation.

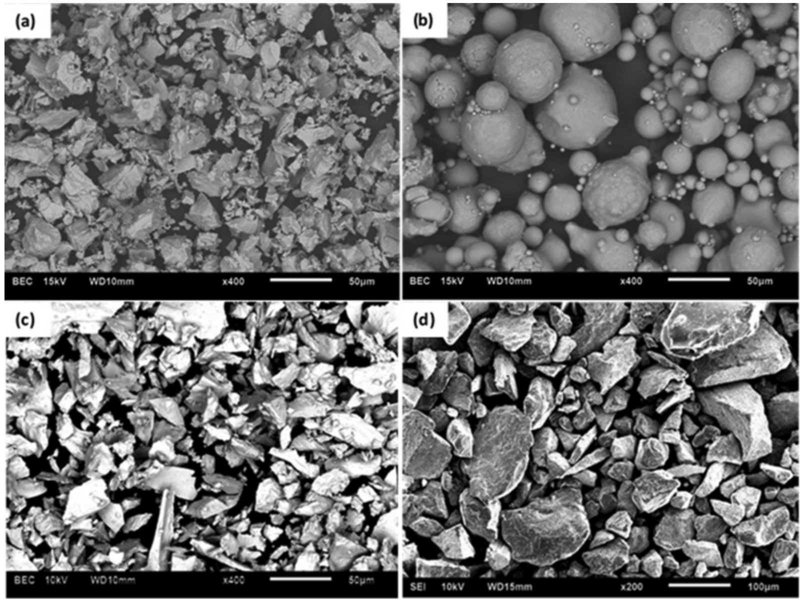

Fig. 1 SEM micrographs of (a) Ti, (b) Al, (c) Nb and (d) Cr powder particles.

Table 2 Particle size and morphology of the powders.

Characteristic	Ti	Al	Nb	Cr
Mean particle size (µm)	30.51	74.0	23.89	126
Morphology	Angular	Spherical	Angular	Angular

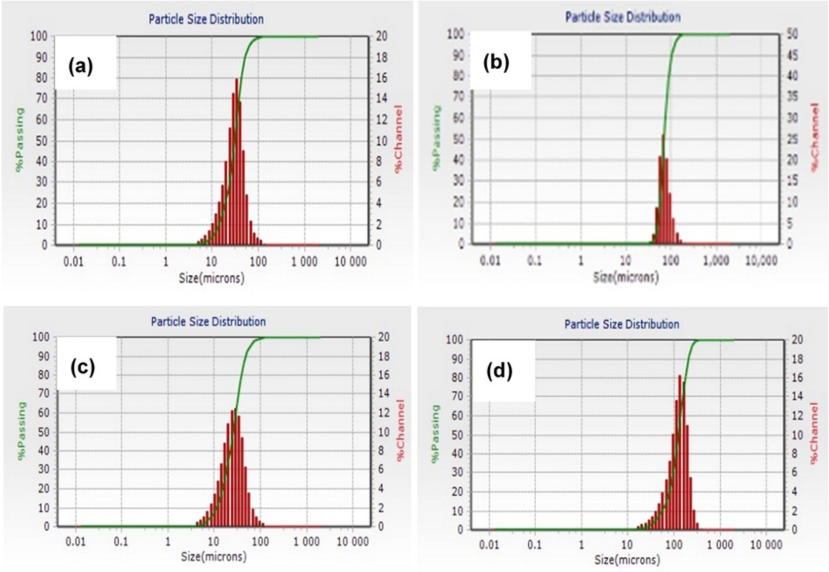

Fig. 2 Particle size distribution of (a) Ti, (b) Al, (c) Nb and (d) Cr powders.

Table 3 Materials constants and properties [11].

Properties	Ti (α)	Al	Nb	Cr
Crystal Structure	HCP	FCC	BCC	BCC
Density (g/cm^3)	4.5	2.7	8.6	7.2
Atomic diameter (nm)	0.289	0.286	0.292	0.260
Melting temperature (°C)	1668	660	2468	1875
Thermal expansion (ppm/°C)	8.4	23.8	7.2	6.5
Yield strength	200	75	170	100

3.2 Uniaxial cold pressing

The three uniaxial cold compressed elemental alloy powder mixture micrographs are shown in Fig. 3a–c. Three 43 mm diameter green compacts representing their corresponding alloys were cross-sectioned and analyzed to determine the effect of cold pressing and chemical homogeneity. In Fig. 3a the cross-sectional micrograph of the binary TiAl powder shows the two-phase structure, the light phase on the surface and dark grey phase towards the centre of the sample. It shows that during cold pressing, there was particle re-arrangement and evidence of particle welding as a result of compaction pressure. The corresponding EDS analysis (insets of Fig. 3) confirmed the high concentration of Al particles on the surface and less towards the centre. This implies that, upon melting the γ-TiAl based alloy compacts, the chemical reaction ignited initially on the surface being the first contact point but also may be due to Al high thermal expansion and low melting temperature shown in Table 3. However, Al will not necessarily melt first but initiates the intermetallic phases as the temperature is increased. Fig. 3**b** represents a ternary TiAlNb elemental powder compact. The Al still dominates the surface due to its spongy characteristics with the presence of a small amount of Nb particles. During cold pressing, the Al particles migrated to the surface in contact with die facets and form a strong weld on particles upon the surface. The quaternary alloy Ti-48Al-2Nb-0.7Cr compact in Fig. 3c followed the similar trend but with no Cr detected on the surface structure.

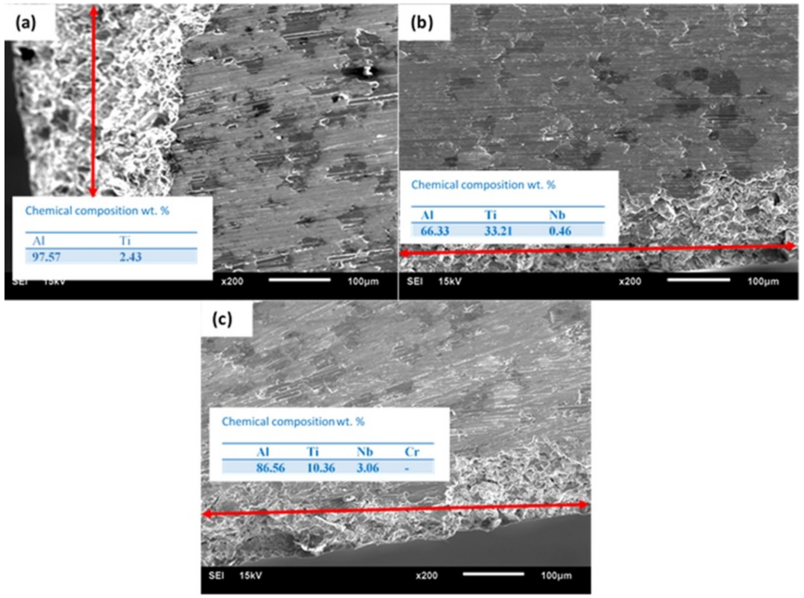

(a) Chemical composition wt. %

Al	Ti
97.57	2.43

(b) Chemical composition wt. %

Al	Ti	Nb
66.33	33.21	0.46

(c) Chemical composition wt. %

Al	Ti	Nb	Cr
86.56	10.36	3.06	-

Fig. 3 SEM/SEI micrographs of (a) Binary Ti-48Al. (b) Ternary Ti-48Al-2Nb and (c) Quaternary Ti-48Al-2Nb-0.7Cr compacted alloy powders.

The composition profile of the compacted alloy powders far away from the surface is illustrated in Figs. 4–6. Supplementary to Fig. 3, the elemental maps with their corresponding percentage composition far away from the surface, indicates that the Al atomic percentage is rather less when compared to the surface of the compact. Moreover, Fig. 6 illustrate that the atomic percentage of Cr is nil, however, in contrast the map profile indicates even distribution of Cr. This may be due to the fact that, the added Cr in the compacted alloy is small about 0.7 percentage atomic.

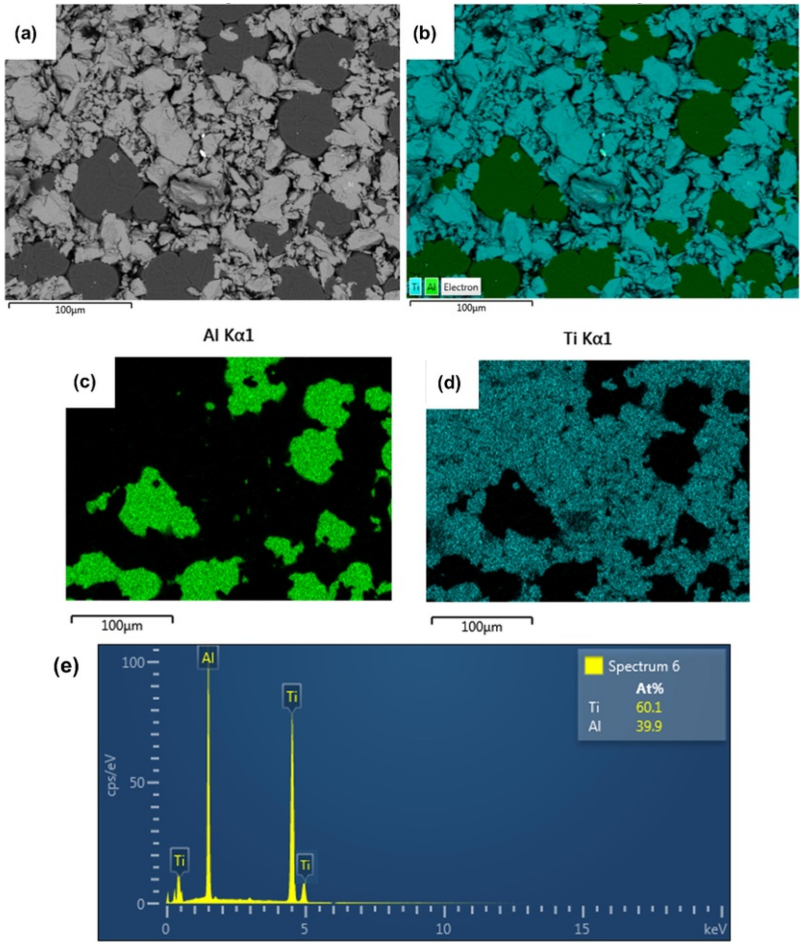

Fig. 4 SEM-EDS elemental map analysis for the Ti-48Al alloy: (a) electron image, (b) EDS layered image, (c) Al Kα, (d) Ti Kα, and (e) spectra with corresponding atomic composition.

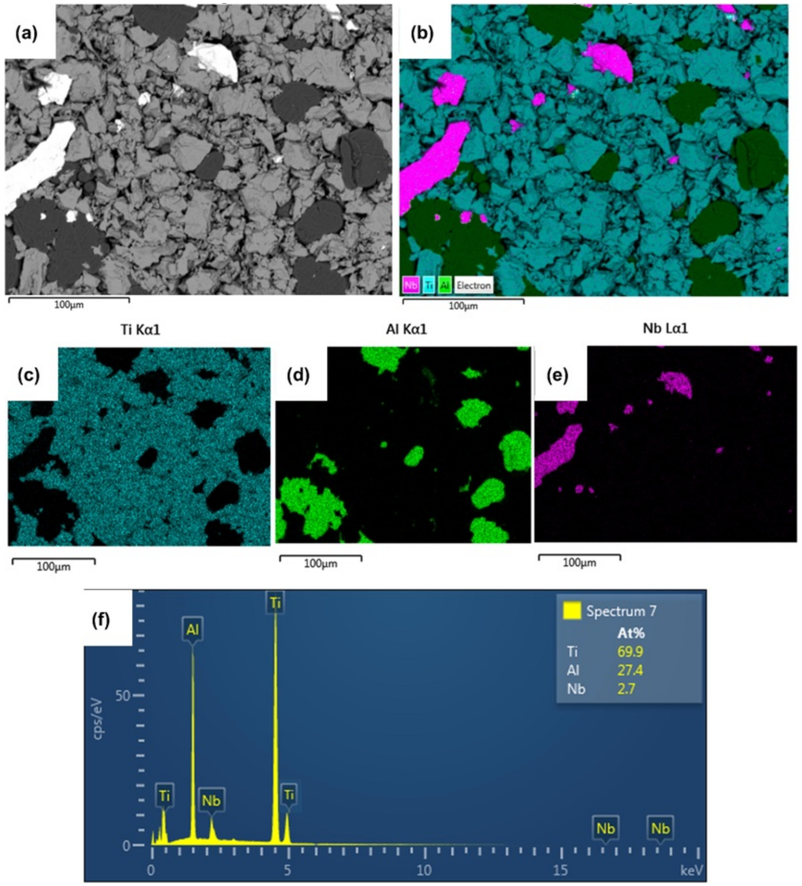

Spectrum 7

	At%
Ti	69.9
Al	27.4
Nb	2.7

Fig. 5 SEM-EDS elemental map analysis for the Ti-48Al-2Nb alloy: (a) electron image, (b) EDS layered image, (c) Ti Kα, (d) Al Kα (e) Nb Kα, and (f) spectra with corresponding atomic composition.

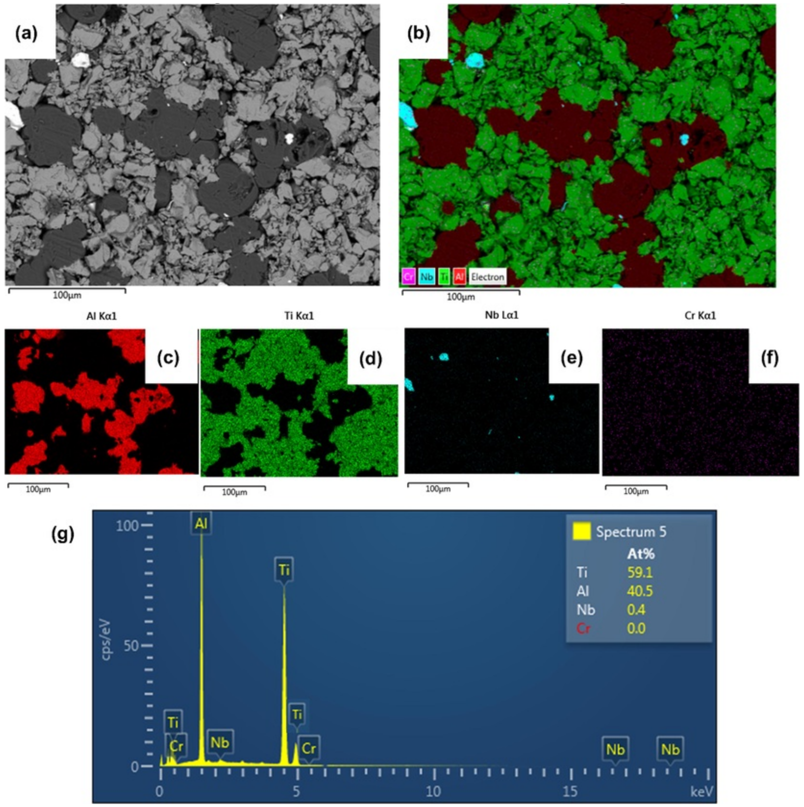

	At%
Ti	59.1
Al	40.5
Nb	0.4
Cr	0.0

Fig. 6 SEM-EDS elemental map analysis for the Ti-48Al-2Nb-0.7Cr alloy: (a) electron image, (b) EDS layered image, (c) Ti Kα, (d) Al Kα (e) Nb Kα, (f) Cr Kα, and (g) spectra with corresponding atomic composition.

As mentioned earlier that the morphology of the elemental powder particles for Ti, Nb, Cr are irregular in shape as indicated in Fig. 1a, c and d, therefore it is observed that the inter-particle voids appear to be more readily closed when compared to the spherical Al powder Fig. 1b. The ability of particles to migrate depend highly upon the cohesive strength of the powder, and powders with little cohesive strength dilate more readily [12]. Ultimately, free flowing blends may segregate readily upon subsequent handling (e.g. mechanical compaction) especially if the different components of the blend do not adhere to one another [12]. Ultimately, air entrainment in the bulk powder blends will result, and cause compaction problems. Prescott and Barnum,[12] reported that as a result of air entrapment, air will flow up and retards the flow of powder, limiting the feed rate. On one hand, the air has a potential to generate erratic flow by fluidizing a portion of the powder in the roll dies; and in this case the Al powder particles.

It is important to note that, the particle size distribution in Fig. 1, and as it was observed that the precursor elemental powders exhibited a considerable size difference between them, and this aids in the average packing densities during compaction, correspondingly [13]. Contrary to this, the minor additions of Nb and Cr to the binary alloy did not have a significant effect on the green compacts, this is indicated by the percentage relative densities Fig. 13, whereby the graph showed a gradually decreasing curve as the alloying elements are added on the green compacts. However, the alloy density after melting, showed improved relative density as the ternary and quaternary elements are added to the binary system.

3.3 XRD pattern analysis

Fig. 8 shows XRD patterns demonstrating lattice planes of the cold pressed γ-TiAl based powder alloys viz. the binary (Ti-48Al), ternary (Ti-48Al-2Nb) and quaternary (Ti-48Al-2Nb-0.7Cr). The HCP-Ti and FCC-Al elemental were detected in the binary alloy shown in Fig. 8a. The lattice parameters of all phases detected are presented in Table 4. For ternary compact powder (Fig. 8b) the minor BCC Nb peaks were detected in agreement with the EDS analysis. On one hand, it is important to note that the powder mixture for the binary, and ternary did not reveal the formation of any new phases as demonstrated by the well defined Al, Ti and Nb peaks, respectively. However, Gabbitas et al. [14] pointed out that it is common to observe a diffraction angle shift of Ti peaks. Surprisingly, the quaternary alloy powder (Fig. 8c) has shown more additional peaks despite the absence of Cr element on the surface in contact with the die, which was also not detected by the EDS analysis. Instead, the rhombohedral (RHL) phase was detected attributed to the change in crystal orientation due to the addition of BCC-Cr elemental on the bulk welded powder. In addition, the compacted powders shown in Fig. 7a–c with their corresponding chemical composition for the γ-TiAl based alloys demonstrate flaky-like particles, which became larger as a result of flattening. This is presumably as a result of cold welding of the elemental crystalline powders during mechanical compaction. The light grey contrast is Ti rich, while the dark contrast is Al rich, in all the alloys in Fig. 7. The pro-found white contrast composition observed in Fig. 7b and c, is an indication of the ternary and quaternary added on the alloys, respectively. It is important to note that, the mechanical compaction in this case, was employed so as to allow the powder particles to deform and alterate from elastic to brittle deformation, in order to constitute bonding between the particles; and not necessarily for alloying. The latter was achieved by melting technique shown by the arc melted buttons with their corresponding EDS chemical analysis in Fig. 9. By contrast, Zambaldi [15] reported that gamma-TiAl has an $L1_0$ structure, which is a tetragonally distorted face-centered cubic lattice, whereby alternate (0 0 2) planes shown in Fig. 8a–c are occupied by the two different species, presented in the work published by Mathabathe et al. [16]. From the discussion therein, strong and anisotropic bonding between Ti atoms on (0 0 1) planes is probably responsible for the c/a ratio being larger than unity in γ-TiAl [15], which is in agreement with $c/a = 1.45$ found in [16].

Table 4 Crystal structure and lattice parameter of TiAl, TiAlNb and TiAlNbCr alloy cold pressed powders.

Alloy	Crystal structure	Space group	Lattice parameters (Å)	
			a	c
Binary	HCP	*P63/mmc # 194*	2.59	4.682
	FCC	*Fm-3m # 225*	4.049	–
Ternary	HCP	*P63/mmc # 194*	2.59	4.682
	FCC	*Fm-3m # 225*	4.049	–
	BCC	*Im3m #229*	3.303	–
Quaternary	HCP	*P63/mmc # 194*	2.591	4.684
	FCC	*Fm-3m # 225*	4.052	–
	BCC	*Im3m #229*	3.303	–
	RHL	*R-3c # 167*	4.994	17.081

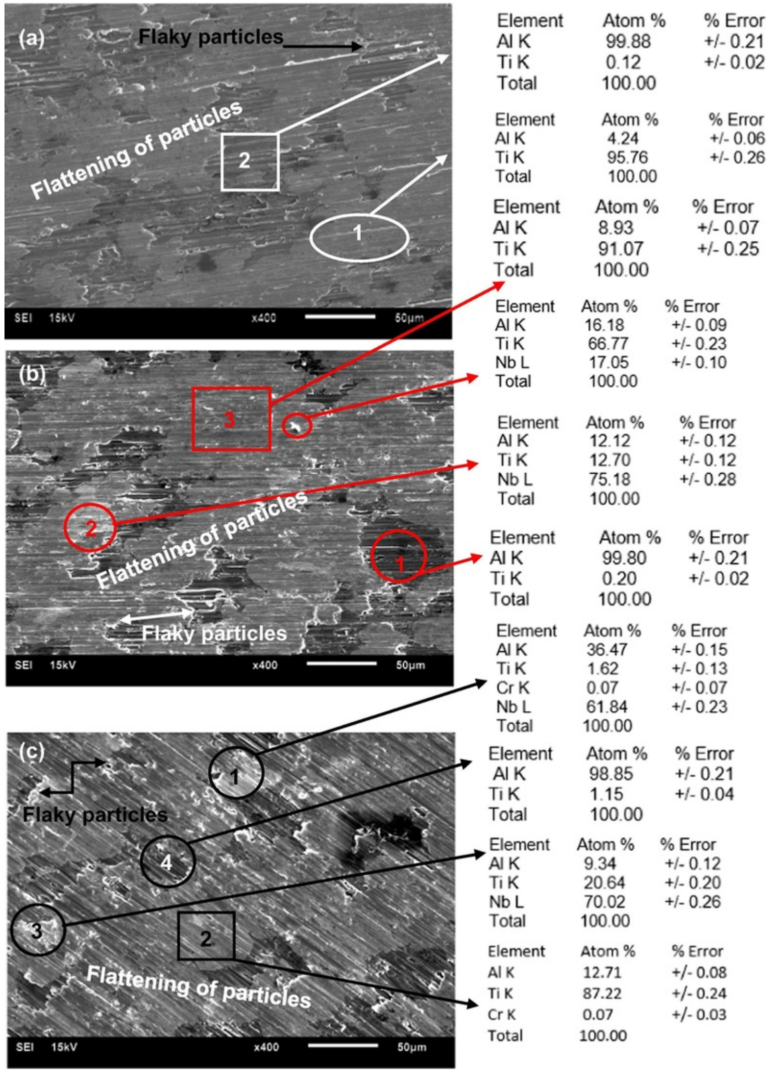

Element	Atom %	% Error
Al K	99.88	+/- 0.21
Ti K	0.12	+/- 0.02
Total	100.00	

Element	Atom %	% Error
Al K	4.24	+/- 0.06
Ti K	95.76	+/- 0.26
Total	100.00	

Element	Atom %	% Error
Al K	8.93	+/- 0.07
Ti K	91.07	+/- 0.25
Total	100.00	

Element	Atom %	% Error
Al K	16.18	+/- 0.09
Ti K	66.77	+/- 0.23
Nb L	17.05	+/- 0.10
Total	100.00	

Element	Atom %	% Error
Al K	12.12	+/- 0.12
Ti K	12.70	+/- 0.12
Nb L	75.18	+/- 0.28
Total	100.00	

Element	Atom %	% Error
Al K	99.80	+/- 0.21
Ti K	0.20	+/- 0.02
Total	100.00	

Element	Atom %	% Error
Al K	36.47	+/- 0.15
Ti K	1.62	+/- 0.13
Cr K	0.07	+/- 0.07
Nb L	61.84	+/- 0.23
Total	100.00	

Element	Atom %	% Error
Al K	98.85	+/- 0.21
Ti K	1.15	+/- 0.04
Total	100.00	

Element	Atom %	% Error
Al K	9.34	+/- 0.12
Ti K	20.64	+/- 0.20
Nb L	70.02	+/- 0.26
Total	100.00	

Element	Atom %	% Error
Al K	12.71	+/- 0.08
Ti K	87.22	+/- 0.24
Cr K	0.07	+/- 0.03
Total	100.00	

Fig. 7 SEM/SEI micrographs of (a) Binary Ti-48Al. (b) Ternary Ti-48Al-2Nb and (c) Quaternary Ti-48Al-2Nb-0.7Cr compacted alloy powders, further away from the surface.

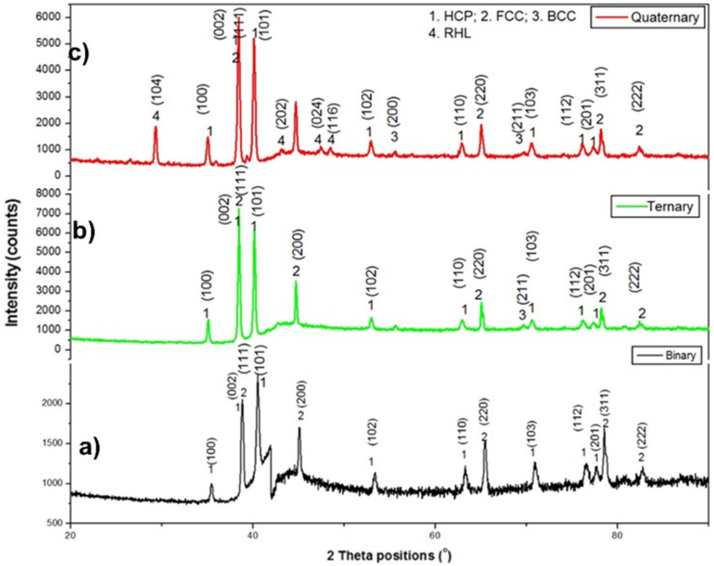

Fig. 8 XRD pattern of TiAl, TiAlNb and TiAlNbCr alloy cold pressed powders.

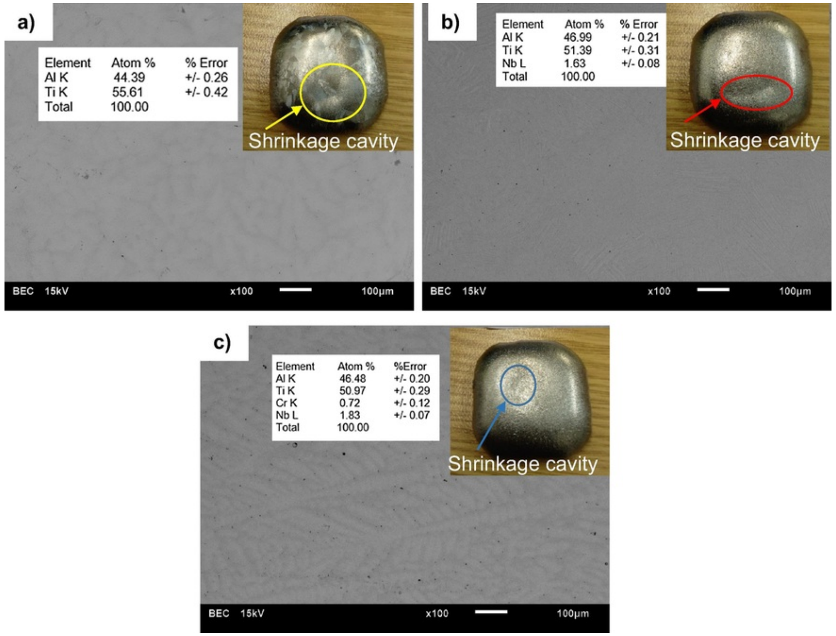

a)

Element	Atom %	% Error
Al K	44.39	+/- 0.26
Ti K	55.61	+/- 0.42
Total	100.00	

b)

Element	Atom %	% Error
Al K	46.99	+/- 0.21
Ti K	51.39	+/- 0.31
Nb L	1.63	+/- 0.08
Total	100.00	

c)

Element	Atom %	%Error
Al K	46.48	+/- 0.20
Ti K	50.97	+/- 0.29
Cr K	0.72	+/- 0.12
Nb L	1.83	+/- 0.07
Total	100.00	

Fig. 9 SEM-BSE micrographs of the arc melted (a) binary, (b) ternary and (c) quaternary alloys with their corresponding as-melted buttons, and EDS chemical analysis.

3.4 As-vacuum button melted microstructure analysis

The microstructures of vacuum arc melted TiAl, TiAlNb and TiAlNbCr alloy are shown in Fig. 9a–c with images of as-cast buttons **(Inset)**, with their corresponding bulk EDS chemical composition which is comparable to the final composition of as-vacuum melted alloy buttons shown in Table 1. The micro-analysis using SEM-EDS illustrate that elemental maps are distributed evenly with the percentage elemental quantity that is more or less than the starting nominal at.% composition, implying the success in the development of the γ-TiAl based alloys via vacuum arc button melting technique for binary, ternary and quaternary alloys, respectively. All the three alloys show dendritic structures associated with micro-segregation of alloying elements. Therefore, the deficiencies of as-cast γ-TiAl based alloys are related not only to the intrinsic brittleness of (γ + α) phases but also to the microstructural evolution of the ingots during solidification. The dendritic colonies in the studied alloys, indicate Al-segregation with dark grey contrast formed in the inter-dendritic regions presumed to have formed during solidification [17].

The binary alloy in Fig. 9a confers a coarse dendritic colony (also shown by macro-etching inset), compared to the ternary and quaternary alloys. The addition of alloying elements (Nb and Cr) induces phase transformation by stabilizing the beta (β) phase in the microstructures, and as a result lead to grain-refinement [8,18]. With subsequent addition of (0.7 at.%) Cr in the ternary Ti-48Al-2Nb alloy Fig. 9b, the as-vacuum melted quaternary Ti-48Al-2Nb-0.7Cr alloy in Fig. 9c shows evidence of new development whereby the dendritic orientation exhibit a fish-bone appearance attributed to a twinning behaviour similar to the one obtained in γ-TiAl based alloys with FCT structure studied by [19]. Moreover, according to Yan et al. [3], micro-segregation of Nb to dendrites occurred during solidification, and a few primary β-phases were retained after cooling to room temperature due to the enrichment of β-phase stabilisers, and this effect is more profound in the quaternary alloy due to both Nb, and Cr contents.

The microanalysis using SEM-EDS illustrated in Figs. 10–12 denotes that elemental maps are distributed evenly with the percentage elemental quantity that is more or less than the starting composition for binary, ternary and quaternary alloys, respectively. On the other hand, it has been shown in our previous study [20] that the as-cast dendritic structures can be altered via thermal treatment in the α-phase domain, in order to produce homogeneous structures consisting of fully lamellar structures with spheroidal and Widmanstätten laths morphology.

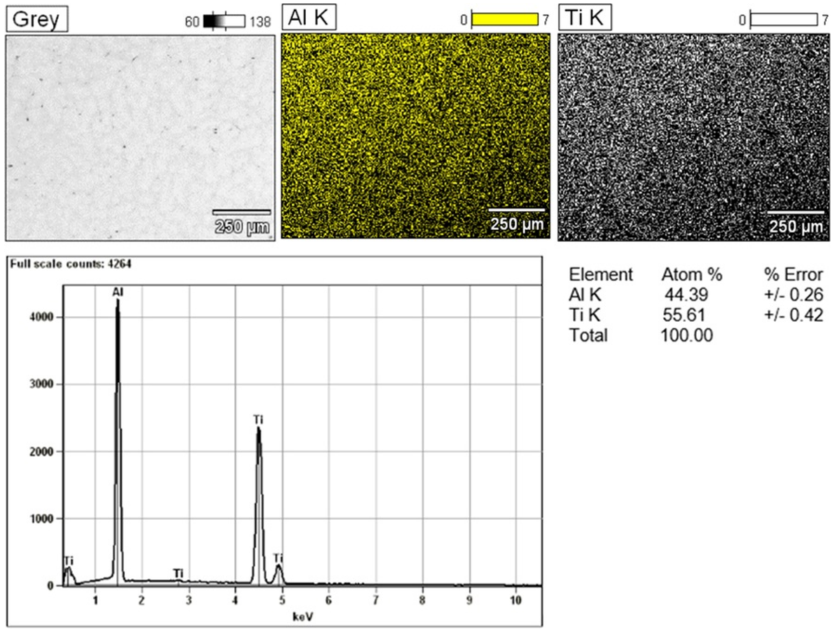

Element	Atom %	% Error
Al K	44.39	+/- 0.26
Ti K	55.61	+/- 0.42
Total	100.00	

Fig. 10 EDS spectra of the melted binary (TiAl) alloy.

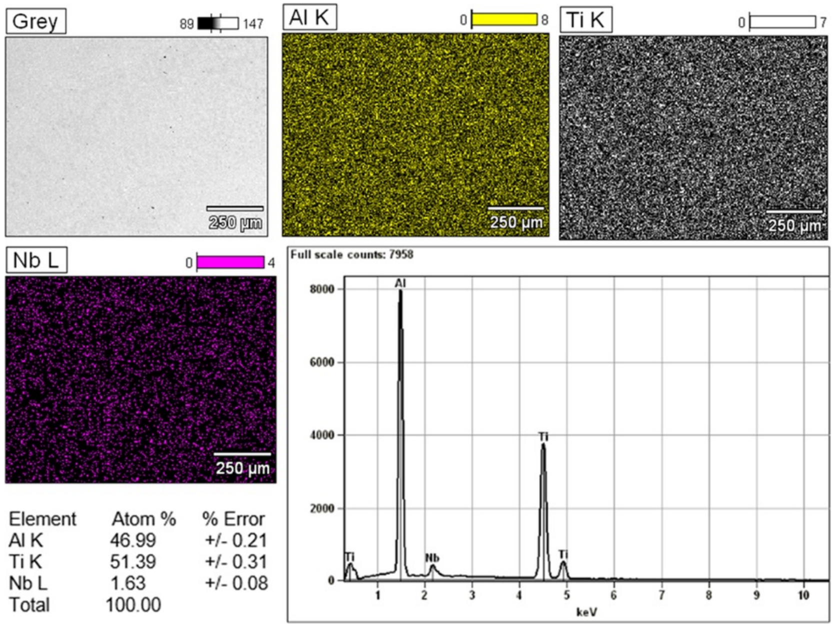

Element	Atom %	% Error
Al K	46.99	+/- 0.21
Ti K	51.39	+/- 0.31
Nb L	1.63	+/- 0.08
Total	100.00	

Fig. 11 EDS spectra of the melted ternary (TiAlNb) alloy.

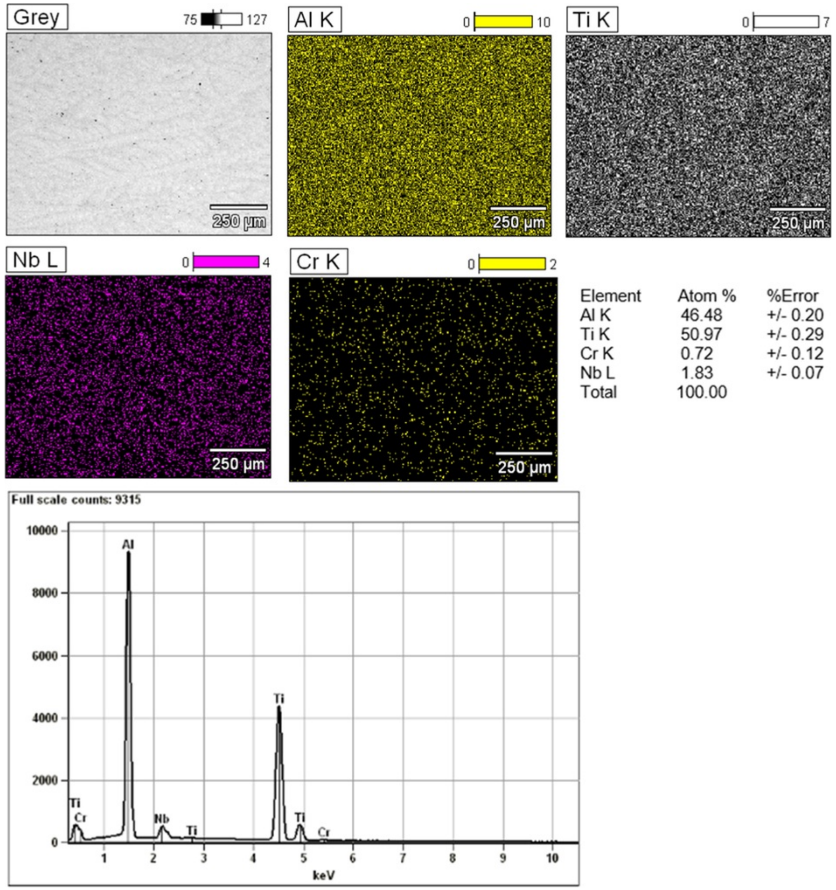

Element	Atom %	%Error
Al K	46.48	+/- 0.20
Ti K	50.97	+/- 0.29
Cr K	0.72	+/- 0.12
Nb L	1.83	+/- 0.07
Total	100.00	

Fig. 12 EDS spectra of the melted quaternary (TiAlNbCr) alloy.

It is noteworthy that one of the most challenging problems in the use of the γ-TiAl based alloys for casting and/or thermo-mechanical processing is the tendency that the ingots can be heterogeneous with varying Al-content of ~1 at.% between top, bottom and across the diameter. However, plasma melting (PM) and vacuum arc remelting (VAR) is able to fabricate homogeneous alloys with no preferential loss of volatile elements such as Al; therefore the resultant ingots have the composition close to the feed stock [21]. It has been shown in this current study that incorporating uniaxial cold pressing for particle bonding with the precursor metallic powder, made the fabrication of the γ-TiAl based alloys successfull via vacuum arc melting with minimum Al-vaporization. Relative densities of the compacted specimens and those of the as-vacuum melted buttons are shown in Fig. 13. The results indicate that the relative densities in the green state are lower compared to the vacuum arc melted buttons. The melting process improved the relative densities by minimising the porosity present on the cold pressed samples shown in Fig. 3a–c. However, emphasis should be made that the as-melted alloys could not achieve 100% densification, which was thought to be attributed to the presence of shrinkage cavities of the alloy buttons indicated in Fig. 9a–c, comprising of a certain amount of pro-eutectoid Al-rich interdendritic γ-phase. The arc melted binary TiAl sample has the lowest relative density compared to the ternary and quaternary sequentially; this may be correlated to the formation of the retained brittle β-phase at room temperature, which is enhanced by the beta stabilizers viz. the Nb and Cr elements, therefore it is presumed that the β/B2 phase is more profound in the quaternary alloy.

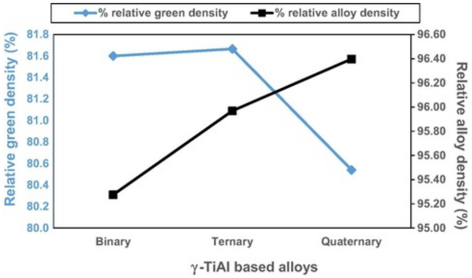

Fig. 13 Comparative relative densities between the green compacts and the arc melted buttons. (For interpretation of the references to colour in this figure legend, the reader is referred to the web version of this article.)

3.5 EBSD analysis

Electron backscattered diffraction (EBSD) mapping has been employed to characterize the as-vacuum melted γ-TiAl based alloys solidified from β-phase domain. The EBSD results revealed that stable phases at room temperature (RT) in the alloys were similar to the one found in our recent study [16], presented in Table 5 which is comparable with experimental data found in [15,22]. Also depicted in Table 5 is the HCP α_2-Ti_3Al with a DO19 –ordered structure, which is formed through an ordering reaction during solidifying of high temperature, disordered α-phase [15].

Table 5 Phase acquisition [16].

Phase Name	a	b	c	α	β	γ	Space group
Alpha	3.20 Å	3.20 Å	5.20 Å	90.00°	90.00°	120.00°	194
(Ti_3Al)	5.72 Å	5.72 Å	4.64 Å	90.00°	90.00°	120.00°	194
Alpha 2	5.73 Å	5.73 Å	4.64 Å	90.00°	90.00°	120.00°	194
Gamma	2.81 Å	2.81 Å	4.08 Å	90.00°	90.00°	90.00°	123

Additional phases substantial at RT in the alloys are illustrated in Table 6. Moreover, the titanium cubic structure was found evident in all the studied alloys meanwhile, the ternary and quaternary alloy exhibited the FCC structure.

Table 6 Phase acquisition of the γ-TiAl based alloys.

Phase Name	a	b	c	α	β	γ	Space group
Titanium cubic	3.19 Å	3.19 Å	3.19 Å	90.00°	90.00°	90.00°	229
Aluminium FCC	4.05 Å	4.05 Å	4.05 Å	90.00°	90.00°	90.00°	225

Figs. 14–16 shows EBSD orientation maps of the as-cast binary (TiAl), ternary (TiAlNb), and quaternary TiAlNbCr alloys. The EBSD results show that the dominant phase in the studied alloys is the γ-phase, indicated by Figs. 14d, 15d, and 16d. Meanwhile, the phase acquisition of the respective alloys is represented in Tables 5 and 6. It is evident that a large number of γ-grains are recrystallized. However, it is shown in Figs. 14c, 15c and 16c that the grain orientation of the recrystallized γ-grains are almost random, which imply that there is no obvious texture attained in the as-cast alloys solidified from β-phase domain, during arc melting technique. The γ-face centered tetragonal structure has $c/a = 1.45$, respectively. Moreover, the identified domain boundaries follow the lines of the band contrast in Figs. 14b, 15b and 16b. The band contrast image for the binary alloy in Fig. 14b display a larger colony size with a full lamellar structure composed of $(\alpha_2 + \gamma)$ which had an average size of about 250 µm. However, the small colony size was the result of β-phase solidification which avoided the peritectic transformation in traditional TiAl alloy which even had a colony size of 1000 µm [23].

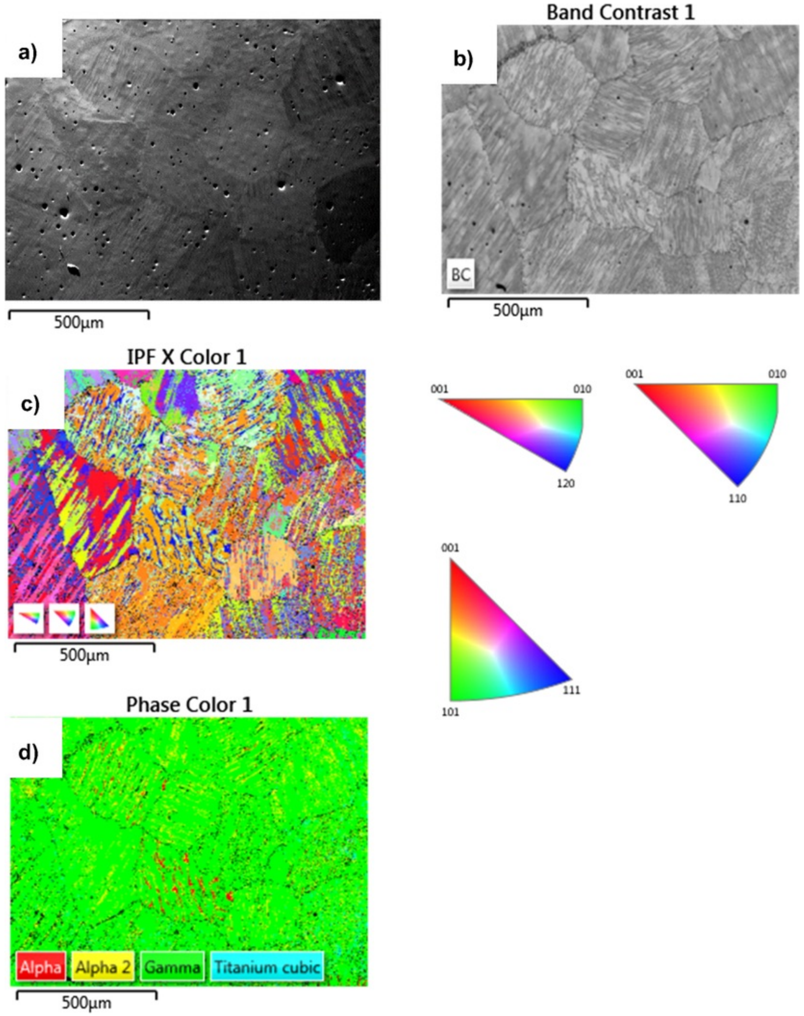

Fig. 14 EBSD maps of the Binary (Ti-44Al) alloy: (a) Electron image; (b) band contrast; (c) inverse pole figure (IPF) maps and (d) phase colour map.

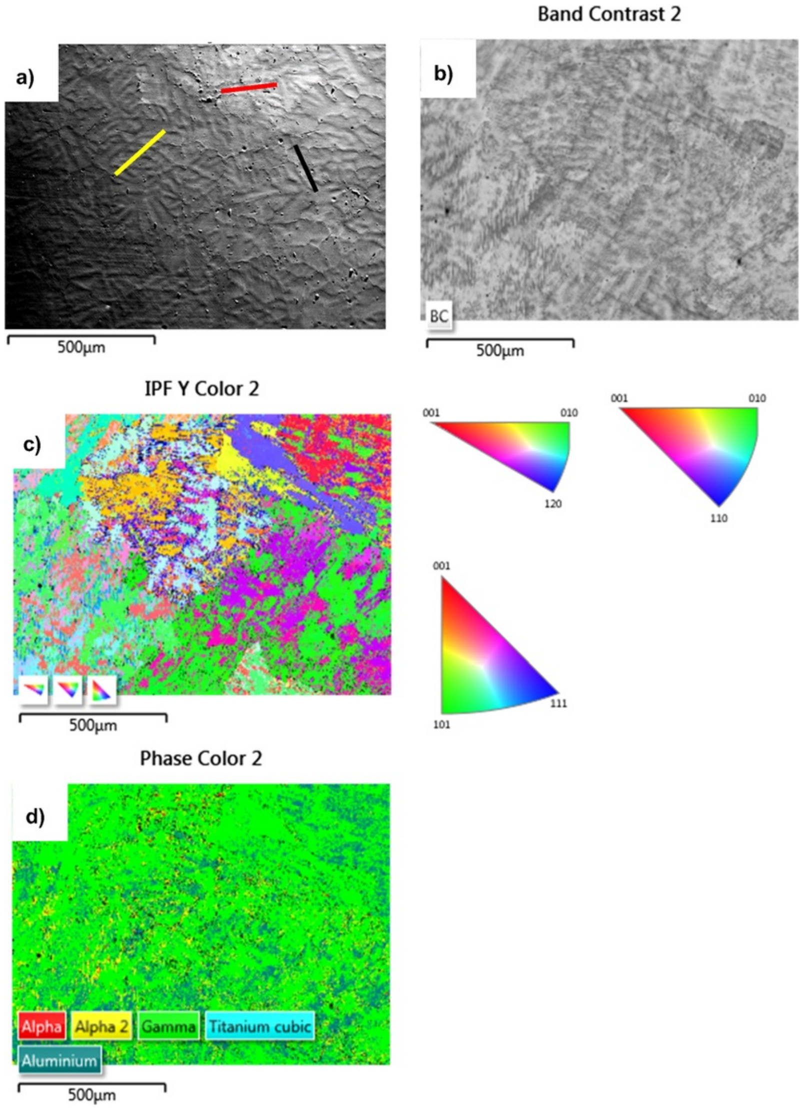

Fig. 15 EBSD maps of the Ternary (Ti-45Al-2Nb) alloy: (a) Electron image; (b) band contrast; (c) inverse pole figure (IPF) maps and (d) phase colour map.

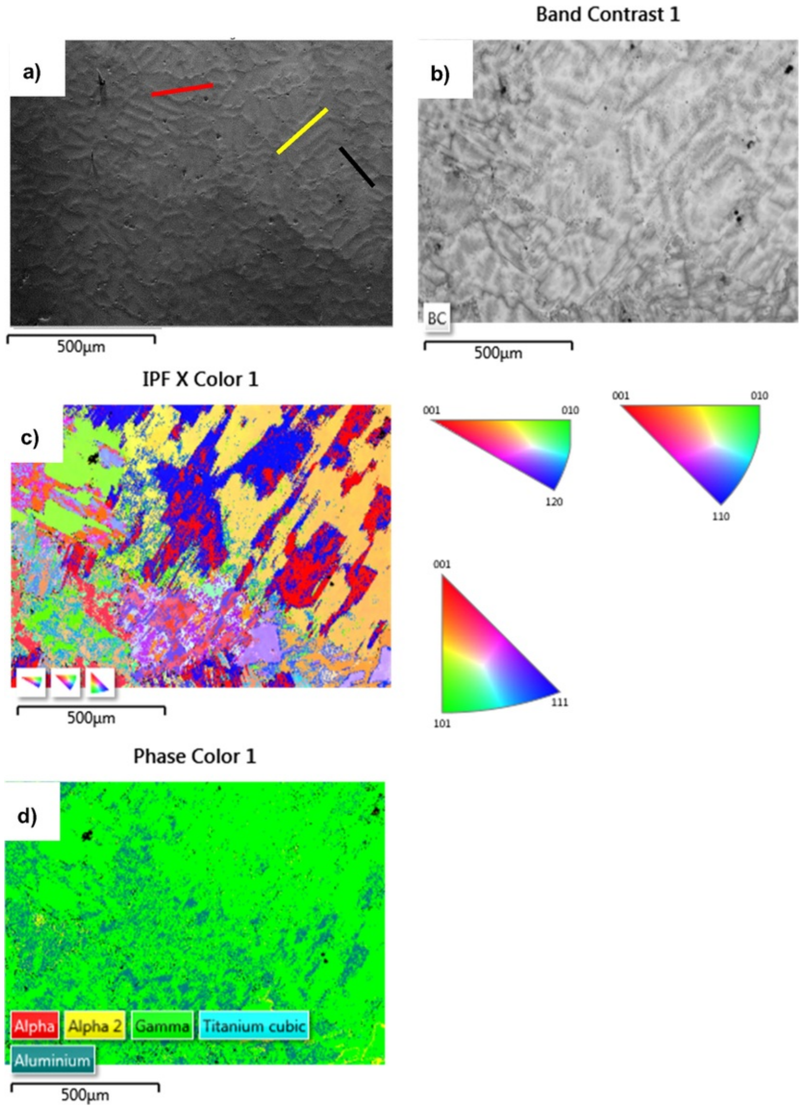

Fig. 16 EBSD maps of the Quaternary (Ti-45Al-2Nb-0.7Cr) alloy: (a) Electron image; (b) band contrast; (c) inverse pole figure (IPF) maps and (d) phase colour map.

Alloying elements such as Nb, Cr, W, Mo are added to TiAl alloys to improve elevated temperature resistance and lamellar structure stability, in addition to stabilizing the β-phase [24,25]. Figs. 15b and 16b show band contrast structures of Ti-45Al-2Nb and Ti-45Al-2Nb-0.7Cr alloys, respectively. It is therefore shown that a large number of β/β_0 phase is distributed at $(\alpha_2 + \gamma)$ lamellar colony boundaries and inside the $(\alpha_2 + \gamma)$ colonies, and consequently divided the large lamellar colonies into many fine lamellar grains when Nb and Cr contents were 2 at.% and 0.7 at.%, respectively. It is important to note that there is no significant difference in the structures between the two alloys, except that the volume fraction of the β/β_0 may be slightly greater than Ti-48Al-2Nb alloy. Furthermore, it was noticed that the electron micrographs in Figs. 15a and 16a exhibited three orientations of the lamellar structure which were at 90°, 45°, and parallel to the primary growth direction of the β-dendrite (the black, red, and yellow lines, which represented the angle of 0°, 45°, and 90°, respectively). As the precipitation of α-phase at the parent β-phase follows a so-called Burgers relationship which was [16]:

$$\{1\,1\,1\}_{\gamma} \parallel (0\,0\,0\,2)_{\alpha} \text{ and } <1\ \bar{1}\ 0>_{\gamma} \parallel <1\,1\ \bar{2}\ 0>_{\alpha}$$

According to Singh et al. [26], the ($\alpha_2 + \gamma$) lamellar structure formed by the reaction of $\alpha \rightarrow \alpha_2 + \gamma$ following the Blackburn orientation relationship has the above three angles with the residual β/β_0-phase. Moreover, the preferential growth of β-phase during solidification is ⟨1 0 0⟩ axis, and the three equivalent directions, namely [1 0 0], [0 1 0] and [0 0 1] are indicated by inverse pole figure maps in Figs. 14c, 15c and 16c [20].

4 Conclusion

The binary (TiAl), ternary (TiAlNb) and quaternary (TiAlNbCr) blended elemental powders were successfully mechanically compacted by uniaxial cold-pressing which constituted bonding between particles whereas alloying was achieved via arc-vacuum melting. The cold pressed samples were sectioned to study the particle arrangement with the SEM/EDS technique. It was evident that the Al particles migrated to the surface in contact with the die surfaces and consequently, the as-cast final composition was indicative of Al vaporization due to vacuum arc melting. The XRD analysis detected elemental Ti, Al, and Nb on binary and ternary samples. However, on the quaternary sample, the rhombohedral phase was detected attributable to the change in crystal orientation due to welding induced by cold pressing. Due to melting, the relative densities of the melted alloys were improved, compared to the green compacted specimens. However, Nb and Cr additions made the relative densities to be slightly higher than that of the binary as a result of the β-phase formation. Compliant to the alloys solidifying from a β-phase domain, EBSD analysis confirmed that the precipitation of α-phase from the parent β-phase followed the Blackburn orientation relationship (BOR), and it was concluded that the primary solidification phase in the alloys was the β-phase. It has been shown in this current study that incorporating uniaxial cold pressing for particle bonding with the precursor metallic powder, made the fabrication of the γ-TiAl based alloys successfull via vacuum arc melting with minimum Al-vaporization. It has been noted that cold pressing of powder can influence the properties of elemental prior to melting [27].

Acknowledgements

Department of Science and Technology (DST) South Africa and Council of Scientific Industrial Research (CSIR) is acknowledged for funding this work. Finally, the technical support from the University of Pretoria mainly for the provision of some of the laboratory equipment’s. We are thankful to Mr Carel Coetzee for EBSD data collection.

References

[1] S. Kumaran, T. Sasikumar, R. Arockiakumar and T. Srinivasa Rao, Nanostructured titanium aluminides prepared by mechanical alloying and subsequent thermal treatment, *Powder Technol.* **185**, 2008, 124–130.

[2] S.R. Dey, A. Hazotte and E. Bouzy, Crystallography and phase transformation mechanisms in TiAl-based alloys – a synthesis, *Intermetallics* **17**, 2009, 1052–1064.

[3] L. Yang, L.H. Chai, Y.F. Liang, Y.W. Zhang, C.L. Bao, S.B. Liu and J.P. Lin, Numerical simulation and experimental verification of gravity and centrifugal investment casting low pressure turbine blades for high Nb–TiAl alloy, *Intermetallics* **66**, 2015, 149–155.

[4] S.F. Franzén, J. Karlsson, γ-Titanium aluminide manufactured by electron beam melting, Masters Dissertation, Gothenburg, Sweden, 2010, p. 81.

[5] S. Lampman, Powder metal technologies and applications, *ASM Int. Mater. Park. OH* **7**, 1998, 716.

[6] Z.Z. Fang, J.D. Paramore, P. Sun, K.S. Ravi Chandran, Y. Zhang, Y. Xia, F. Cao, M. Koopman and M. Free, Powder metallurgy of titanium – past, present, and future, *Int. Mater. Rev.* 2017, 1–53.

[7] R. Schafrik and R. Sprangue, Gas turbine materials part Π, *Adv. Mater. Process.* 2004, 22–23.

[8] Z.Z. Shen, J.P. Lin, Y.F. Liang, L.Q. Zhang, S.L. Shang and Z.K. Liu, A novel hot pack rolling of high Nb e TiAl sheet from cast ingot, *Intermetallics* **67**, 2015, 19–25.

[9] M.N. Mathabathe, A.S. Bolokang, G. Govender, R.J. Mostert and C.W. Siyasiya, The vacuum melted ɣ-TiAl (Nb, Cr, Si)-doped alloys and their cyclic oxidation properties, *Vacuum* **154**, 2018, 82–89.

[10] M.N. Mathabathe, G. Govender, C.W. Siyasiya, R.J. Mostert and A.S. Bolokang, Surface characterization of the cyclically oxidized γ-Ti-48Al-2Nb-0.7Cr alloy after nitridation, *Mater. Charact.* **154**, 2019, 94–102.

[11] R. German, Powder metallurgy science, *Met. Powder Ind. Fed. Princet.* 1994, 279.

[12] J. Prescott and R. Barnum, On powder flowability, *Pharm. Technol.* **24**, 2000, 60–84.

[13] H.W. Liu and K.P. Plucknett, Titanium aluminide (Ti-48Al) powder synthesis, size refinement and sintering, *Adv. Powder Technol.* **28** (1), 2017, 314–323.

[14] B. Gabbitas, P. Cao, S. Raynova and D. Zhang, Microstructural evolution during mechanical milling of Ti/Al powder mixture and production of intermetallic TiAl cathode target, *J. Mater. Sci.* **47** (3), 2012, 1234–1243.

[15] C.R. Zambaldi, Micromechanical modeling of γ-TiAl based alloys, PhD Dissertation, Deutschen Nationalbibliografie, 2010, pp. 1–201.

[16] M.N. Mathabathe, A.S. Bolokang, G. Govender, R.J. Mostert and C.W. Siyasiya, Structure-property orientation relationship of a $\gamma/\alpha_2/Ti_5Si_3$ in as-cast Ti-45Al-2Nb-0.7Cr-0.3Si intermetallic alloy, *J. Alloys Compd.* **765**, 2018, 690–699.

[17] X.F. Ding, J.P. Lin, L.Q. Zhang, H.L. Wang, G.J. Hao and G.L. Chen, Microstructure development during directional solidification of Ti-45Al-8Nb alloy, *J. Alloys Compd.* **506**, 2010, 115–119.

[18] G. Yang, H. Kou, J. Yang, J. Li and H. Fu, Microstructure control of Ti-45Al-8.5Nb-(W, B, Y) alloy during the solidification process, *Acta Mater.* **112**, 2016, 121–131.

[19] G. Liu, Z. Wang, T. Fu, Y. Li, H. Liu, T. Li, M. Gong and G. Wang, Study on the microstructure, phase transition and hardness for the TiAl-Nb alloy design during directional solidification, *J. Alloys Compd.* **650**, 2015, 45–52.

[20] M.N. Mathabathe, S. Govender, A.S. Bolokang, R.J. Mostert and C.W. Siyasiya, Phase transformation and microstructural control of the alpha-solidifying ɣ-Ti-45Al-2Nb-0.7Cr-0.3Si intermetallic alloy, *J. Alloys Compd.* **757** 2018, 8–15.

[21] X. Wu, Review of alloy and process development of TiAl alloys, *Intemetallics* **14**, 2006, 1114–1122.

[22] C.Z. Qiu, Y. Liu, L. Huang, B. Liu, W. Zhang, Y. He and B. Huang, Tuning mechanical properties for (B2)-containing TiAl intermetallics, *Trans. Nonferrous Met. Soc.* **22**, 2012, 2593–2603.

[23] S.Z. Zhang, Y.B. Zhao, C.J. Zhang, J.C. Han, M.J. Sun and M. Xu, The microstructure, mechanical properties, and oxidation behavior of beta- gamma TiAl alloy with excellent hot workability, *Mater. Sci. Eng. A* **700**, 2017 366–373.

[24] T. Liu, L.S. Luo, D.H. Zhang, L. Wang, X.Z. Li, R.R. Chen, Y.Q. Su, J.J. Guo and H.Z. Fu, Comparison of microstructures and mechanical properties of as-cast and directionally solidified Ti-47Al-1W-0-5Si alloy, *J. Alloys Compd.* **682**, 2016, 663–671.

[25] A.V. Kartavykh, E.A. Asnis, N.V. Piskun, I.I. Statkevich, A.A. Stepashkin, M.V. Gorshenkov and T.K. Akopyan, Complementary thermodynamic and dilatometric assessment of phase transformation pathway in new beta-stabilized TiAl intermetallics, *Mater. Lett.* **189**, 2017, 217–220.

[26] A.K. Singh, K. Muraleedharan and D. Banerjee, Solidification structure in a cast γ alloy, *Scr. Mater.* **48**, 2003, 767–772.

[27] A.S. Bolokang, M.J. Phasha, D.E. Motaung and S. Bhero, Effect of mechanical milling and cold pressing on Co powder, *J. Metallurg.* **2012**, 2012, 1–7, https://doi.org/10.1155/2012/290873.

Graphical abstract

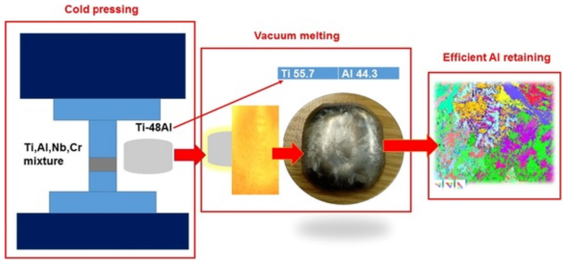

Highlights

- Development of γ-based TiAl-doped with Nb, Cr alloys was studied.
- The study showed that the alloy solidified by $L + \beta \rightarrow \alpha$ peritectic reaction.
- Subsequent phase transformation occurring by α (hcp) $\rightarrow \alpha + \beta \rightarrow \alpha_2$ (DO_{19}) $+ \gamma$ ($L1_0$).
- Blackburn orientation relationship is ensued by $\alpha \rightarrow \alpha_2$ ordering reaction.